ADVANCED MATERIALS
www.advmat.de

Topological Spin Textures in an Insulating van der Waals Ferromagnet

Sergey Grebenchuk, Conor McKeever, Magdalena Grzeszczyk, Zhaolong Chen, Makars Šiškins, Arthur R. C. McCray, Yue Li, Amanda K. Petford-Long, Charudatta M. Phatak, Duan Ruihuan, Liu Zheng, Kostya S. Novoselov, Elton J. G. Santos,* and Maciej Koperski**

Generation and control of topological spin textures constitutes one of the most exciting challenges of modern spintronics given their potential applications in information storage technologies. Of particular interest are magnetic insulators, which due to low damping, absence of Joule heating and reduced dissipation can provide energy-efficient spin-textures platform. Here, it is demonstrated that the interplay between sample thickness, external magnetic fields, and optical excitations can generate a prolific paramount of spin textures, and their coexistence in insulating $CrBr_3$ van der Waals (vdW) ferromagnets. Using high-resolution magnetic force microscopy and large-scale micromagnetic simulation methods, the existence of a large region in *T-B* phase diagram is demonstrated where different stripe domains, skyrmion crystals, and magnetic domains exist and can be intrinsically selected or transformed to each-other via a phase-switch mechanism. Lorentz transmission electron microscopy unveils the mixed chirality of the magnetic textures that are of Bloch-type at given conditions but can be further manipulated into Néel-type or hybrid-type via thickness-engineering. The topological phase transformation between the different magnetic objects can be further inspected by standard photoluminescence optical probes resolved by circular polarization indicative of an existence of exciton-skyrmion coupling mechanism. The findings identify vdW magnetic insulators as a promising framework of materials for the manipulation and generation of highly ordered skyrmion lattices relevant for device integration at the atomic level.

1. Introduction

Over the past few years skyrmions became an extensively researched topic in magnetism. As they present themselves as topological magnetic objects, they hold great promise as potential building blocks for new memory devices (like racetrack memory), neuromorphic computing, and other spintronics application due to their stability and specific characteristics.[1–4] Skyrmions are usually observed in chiral,[5–7] polar[8–15] magnets as well at interfaces[1] where Dzyaloshinskii–Moriya interaction (DMI) is sizeable. This interaction is responsible for the spin canting of the textures and favors the formation of chiral bubbles within the right combination of crystal structure (e.g., non-centrosymmetric) and magnetic parameters (e.g., spin anisotropy, exchange constants, and dipolar interactions). In many instances most of the materials hosting such magnetic objects are metallic thin films[6,16–18] and metal/heavy metal hetero-structures[1,8,9,11] that intrinsically suffer from high heat generation and Ohmic losses due to the conduction electrons when used in memory

S. Grebenchuk, M. Grzeszczyk, Z. Chen, M. Šiškins, K. S. Novoselov, M. Koperski
Institute for Functional Intelligent Materials
National University of Singapore
Singapore 117544, Singapore
E-mail: sergey.g@u.nus.edu; msemaci@nus.edu.sg

S. Grebenchuk, K. S. Novoselov, M. Koperski
Department of Materials Science and Engineering
National University of Singapore
Singapore 117575, Singapore

The ORCID identification number(s) for the author(s) of this article can be found under https://doi.org/10.1002/adma.202311949

DOI: 10.1002/adma.202311949

C. McKeever, E. J. G. Santos
Institute for Condensed Matter Physics and Complex Systems
School of Physics and Astronomy
The University of Edinburgh
Edinburgh EH9 3FD, UK
E-mail: esantos@exseed.ed.ac.uk

A. R. C. McCray, Y. Li, A. K. Petford-Long, C. M. Phatak
Materials Science Division
Argonne National Laboratory
Lemont, IL 60439, USA

A. R. C. McCray
Applied Physics Program
Northwestern University
Evanston, IL 60208, USA

applications. In this context, semiconducting and insulating compounds with electronic bandgaps[10,19–22] might provide an energy-efficient solution despite of additional phenomena through topological insulator properties.[2] However, most of the insulators developing spin-textures show complex crystal structure and chemical properties (e.g., $VOSe_2O_5$, GaV_4Se_8, GaV_4S_8, Cu_2OSeO_3) that hamper practical implementations in ultrathin, open-source, low power-consumption skyrmionic platforms.

2D vdW magnetic layers demonstrated a number of peculiar properties[23–27] not present in materials exhibiting uniquely covalent or ionic bonds. The 2D systems offered a fruitful realm of investigations of magnetic phenomena at different phases, atomic thicknesses, and under different external excitations not easily accessible or achievable in more conventional magnetic crystals. Recently, a few vdW magnets, i.e., $Fe_{3-x}GeTe_2$, $Fe_{5-x}GeTe_2$,$Cr_2Ge_2Te_6$, and $CrCl_3$, demonstrated the possibility of sustaining topological spin textures[13,14,28–33] under different scenarios from magnetic bubbles,[34,35] stripe domains[36] up to topological quasiparticles, such as skyrmions[13,14,29,31,37–39] and merons.[30,32] These evidences provide a vast territory for exploration either in more fundamental levels, in terms of the basic interactions dictating the formation of magnetic textures in confined two-dimensions, or in functional applications where the control of spin textures in devices is the ultimate step. It is a common supposition that the formation of chiral spin structures is generally more prone to crystals without space inversion symmetry where substantial DMI can be developed. Similar approach is also valid for vdW interfaces where the lack of inversion symmetry gives rise to interfacial DMI whose magnitude may be enhanced by the spin-orbit coupling from the underneath substrate.[28,40] These non-centrosymmetric guidelines liaised with the presence of DMI have been influencing the search of topological spin textures broadly. However, recent experimental investigations proved the possibility of skyrmion formation in centrosymmetric 2D crystals.[13,14,27,31–33,41] Indeed, it is unclear whether materials holding spatial inversion symmetry, negligible DMI and displaying insulating or semiconducting properties can generate spin textures under different driving forces (e.g., magnetic fields, currents). Moreover, the use of common light probes of continuous wave excitation (non-time resolved) to inspect, generate, and manipulate topological spin objects on 2D vdW compounds has so far been elusive.

Here, we showed that insulating $CrBr_3$ vdW ferromagnet constitutes such an unconventional skyrmionic system with a high degree of tunability with magnetic fields, temperature gradients, and laser excitations. Using low-temperature magnetic force microscopy (MFM), Lorentz transmission electron microscopy (LTEM), and photoluminescence (PL) spectroscopy measurements, we demonstrated that several magnetic phases involving skyrmions and stripe domains coexist. Upon variation of temperature, magnetic field, and sample thickness, the topological character of the textures itself can be manipulated inducing the formation of ordered skyrmion lattices of different types, e.g., Bloch, Néel and hybrids, and their reversible transformation. Micromagnetic simulations reproduce closely the variety of magnetization textures in different physical conditions and point to the cooperative effect between dipolar interactions, spin anisotropy, and exchange fields as the main driving force for the phase transformation. This magnetic-texture-switch process occurs at almost the entire range of temperatures where $CrBr_3$ is magnetic and provides a practical approach to create, detect, and manipulate information with topological characteristics.

2. Results

2.1. Stripe Domains, Skyrmion Crystal, and Chirality

In this study, we inspected the magnetic and optoelectronic properties of mechanically exfoliated $CrBr_3$ films deposited on SiO_2/Si substrate. The magnetization textures forming in the samples were inspected via high resolution (30 nm) MFM as well as by LTEM at cryogenic temperatures. As expected in ferromagnetic materials, the magnetic domains in $CrBr_3$ depended on the history of the previously applied magnetic field at varying temperatures. When the sample was cooled down to the base temperature of 1.7 K in zero-field cooling (ZFC) mode, the $CrBr_3$ films adopted a ground state characterized by stripe magnetic domains (**Figure 1a**). Such configuration is typical for materials with an out-of-plane easy axis of magnetization.[14,27,34] The structure also had magnetic bubbles, and donut-like magnetic structures interacting with curled stripe domains in contrast to monodomains commonly found in 2D magnets[34,42,43] in the limit of atomic thickness. The magnetic textures dominated by stripe patterns barely changed under the influence of external magnetic fields. The domains slightly increased or decreased their size at an applied magnetic field (50 mT in Figure 1b) but their geometry remained mostly unaffected. Only fields close to saturation (>150 mT) were able to create bubbles or substantially modify the stripe domains initially stabilised via ZFC (Figure S4, Supporting Information). This implies formation of highly stable magnetic ground state resilient against thermal and field perturbations for the stripe domain patterns.

The magnetic configurations were starkly different upon field-cooling (FC) procedures. The FC magnetic field of 50 mT triggered a nucleation and growth of a skyrmion crystal (SkX) with a well ordered hexagonal lattice (Figure 1c). The perfect periodic arrangement of the skyrmions was confirmed via the fast Fourier transformed (FFT) image (Figure 1d) that demonstrated

A. K. Petford-Long, C. M. Phatak
Department of Materials Science and Engineering
Northwestern University
Evanston, IL 60208, USA
D. Ruihuan, L. Zheng
School of Materials Science and Engineering
Nanyang Technological University
Singapore 639798, Singapore
D. Ruihuan
CINTRA CNRS/NTU/THALES, UMI 3288, Research Techno Plaza
Nanyang Technological University
Singapore 639798, Singapore
E. J. G. Santos
Higgs Centre for Theoretical Physics
The University of Edinburgh
Edinburgh EH9 3FD, UK
E. J. G. Santos
Donostia International Physics Center (DIPC)
20018 Donostia-San Sebastián
Basque Country Spain

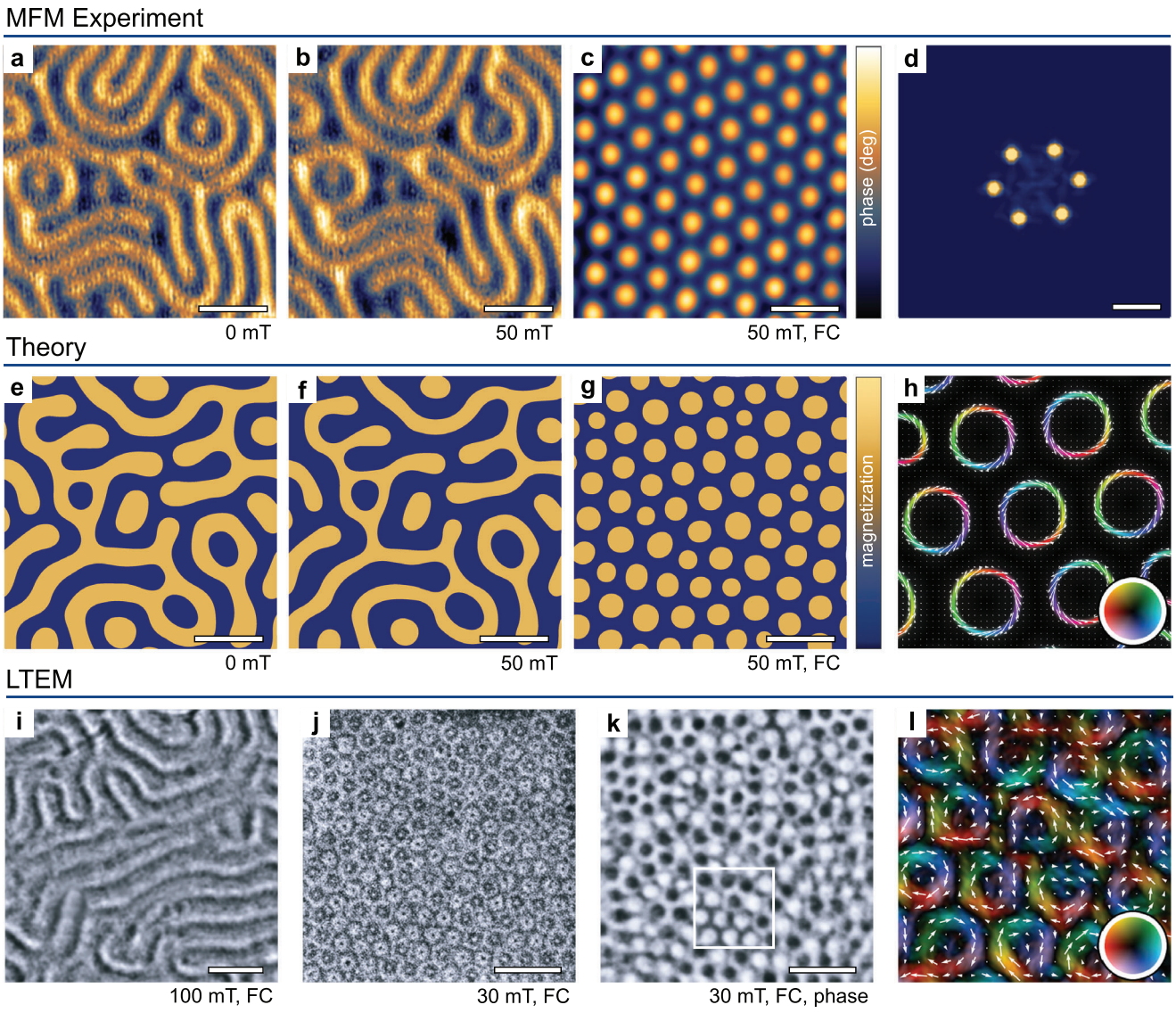

Figure 1. Skyrmion lattice in $CrBr_3$. a–c) Experimental magnetic force microscopy (MFM) images of the magnetic structures stabilised in $CrBr_3$ at various field conditions at 1.68 K. Stripe domains (a) were obtained at zero field cooling (ZFC), and were very stable under applied fields (50 mT in b) once they were initially created in (a). Nucleation of a skyrmion lattice (c) was achieved through field cooling (FC) at 50 mT. In the MFM measurements, the tip was kept at 40 nm distance away from the sample surface. d) Fast Fourier transform (FFT) pattern of (c) demonstrated the highly ordered hexagonal arrangement of the skyrmion achieved via FC-diven lattice growth. e–g) Micromagnetic simulation revealed the magnetization textures of the system at the same conditions as in the experimental MFM images in (a–c), respectively. h) Local view of the demagnetizing field along in-plane components of the magnetization ($M_{x,y}$) is shown for skyrmions from (g). The variations of $M_{x,y}$ along the bubbles indicated Bloch-type skyrmions (Figure S12, Supporting Information). i) Lorentz transmission electron microscopy (LTEM) image of stripe domains was recorded with defocus length $\Delta z = -2$ mm after FC the sample to 13 K in a 100 mT out-of-plane field. j) LTEM image of bubble domains was recorded with $\Delta z = -0.7$ mm after FC the sample to 14 K in a 30 mT field. k) Reconstructed phase map of (j) showed clear Bloch bubble domains characterised by mixed chirality. l) In-plane magnetic induction map of the boxed region indicated in (k). The white scale bar on (a–c), (e–g), and (i–k) corresponds to 0.5 µm, whereas on the FFT pattern in (d) it corresponds to 5 μm^{-1}. The MFM measurements and simulations were done for 175 nm thick $CrBr_3$ film, LTEM - for 110 nm thick sample.

a hexagon in the inverse space indicative of ordered spin quasi-particles with a lattice spacing of ~250 nm. The statistical distribution of the skyrmion sizes revealed small variations of their diameters (120–130 nm for 175 nm thick $CrBr_3$ films). Rarely, individual larger skyrmions exceeding significantly the typical size for a particular thickness of the $CrBr_3$ film had emerged (see **Figure** 2e–g; Figure S7, Supporting Information). These irregularities induced the formation of magnetic vacancies in their vicinity, leading to distortions and defects in the overall skyrmion lattice. Notably, these magnetic vacancies were not associated with inherent crystalline defects or pinning sites intrinsically present in ferromagnetic crystals. Instead, they are associated to the reconstruction of the skyrmionic lattices after thermal cycling with the initial formation of stripe domains of different widths but evolving into localised spin textures of different sizes.

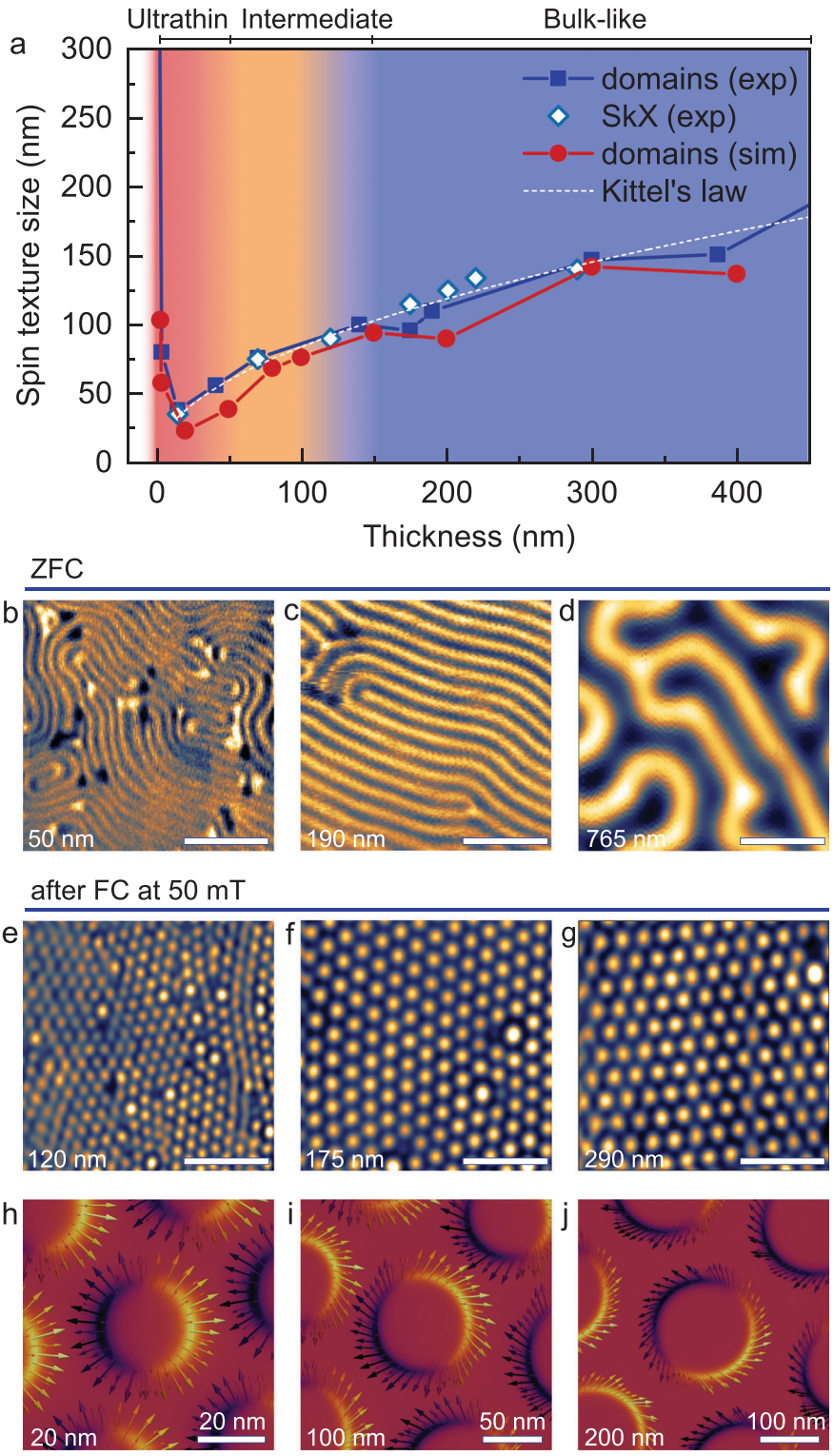

Figure 2. Thickness-dependent spin textures. a) Spin textures sizes versus film's thickness for magnetic domains (blue dots), skyrmion crystals - SkX (white dots) obtained from MFM measurements and micromagnetic simulations (red dots). The trend arising from Kittel's law (dashed line) is presented as a frame of reference. Three different regimes hosting different types of skyrmions at varied thickness were identified: ultrathin, intermediate and bulk-like. b–d) MFM scans of the stripe domains for samples with different thicknesses (50 nm, 190 nm, 765 nm) at ZFC, respectively. e–g) Skyrmion lattice obtained for samples with different thicknesses (120, 170, and 290 nm) after FC at 50 mT, respectively. The scale bar in all MFM images (b–g) corresponds to 1 µm. MFM measurements were done at 1.67 K. h–j) Simulated topological textures at 1.67 K for different thicknesses (20, 100, and 200 nm) demonstrated Néel-like, hybrid and Bloch-like skyrmions, respectively.

To provide further understating of the formation of the stripe magnetic domains and skyrmions in $CrBr_3$, we have undertaken large-scale micromagnetic simulations including the fundamental interactions in the spin Hamiltonian: the exchange energies, magnetic anisotropy, DMI, and dipolar interactions (see Experimental Section for the details of the computational procedures). In the calculations, we mimicked the experimental protocols defining the history of the samples exposure to similar physical conditions. That is, we began from a randomized spin state at the temperature significantly exceeding the Curie temperature (T = 200 K), and slowly cooled down the system in steps of 5 K for 10 ns at each step in the absence or presence of a magnetic field. The total computation time for each simulation was within 400–1000 ns, which guarantees that each ground-state is fully converged. Strikingly, we could reproduce qualitatively similar features of the magnetic textures as observed experimentally (Figure 1e–h). The simulations captured the formation of the stripe domains, skyrmion lattice with different texture sizes, modifications of the stripe domain patterns with magnetic field, and the high stability of the magnetic ground-state with the applied field. The simulated magnetic textures were sensibly dependent on the inclusion of magnetic fields during field cooling at various initial temperatures considered.

We found that the skyrmions nucleated randomly over the $CrBr_3$ film (Figure 1g,h), and their distribution over the skyrmion lattice occurred stochastically following the energy minimization of the system. The different skyrmion size as observed in the measurements was remnant of the different widths of the stripe domains initially created at early stages of the thermal equilibration but evolved into localized bubbles and skyrmions afterward. The formation of skyrmions and SkX via FC procedures was due to the competition of dipolar fields and exchange energy throughout the surface. Figure S13 (Supporting Information) shows that DMI has a marginal effect on the formation of topological spin textures in $CrBr_3$ as the skyrmion lattice emerged in its absence. This observation became more pronounced in the films of increasing thickness (beyond 50–70 nm) as dipole–dipole interactions were found to play a dominant role in the formation of the magnetic order. DMI was found necessary to reproduce the evolution of the size of the stripe domains and skyrmions with an applied magnetic field, but it was not the driving factor in their formation. The skyrmion chirality was elucidated by LTEM measurements (Figure 1i–l). Through phase-contrast electron microscopy of spin textures, we replicated the images of stripe domains and SkX similarly as in the MFM probing, but with an additional information about local spin orientations in terms of the mixed chirality of the skyrmions (Figure 1j,k). Skyrmions with opposite chiralities (seen in LTEM images as dark and bright disks) were generated in $CrBr_3$ exhibiting a disordered pattern. In certain regions of the sample, local chirality common to a few skyrmions is stabilized at short length-scales (< 0.7 μm) in the form of clusters of co-oriented skyrmions. At the thickness studied in LTEM experiments (≈110 nm), the skyrmions manifested as quasiparticles consistent with Bloch-type spin textures in agreement with micromagnetic simulations (Figure S13, Supporting Information). In these textures, the spins wrap clockwise or counter-clockwise around the skyrmion core (Figure 1h,l) depending on the balance of the different interactions involved. The calculation of the topological charge S_{Sk} (Figure S15, Supporting Information) resulted in a magnitude of $S_{Sk} \approx -0.97$ per bubble, demonstrating that the simulated textures are close to a perfect skyrmion scenario. However, the mixed chiralities due to weak DMI contributions imply that the magnetic textures in the investigated samples might also be associated to skyrmionic bubbles with an enlarged core compared to an ideal skyrmion.[44] In this case, the mixed chirality would follow the dipolar interactions present in the system, since a single helicity due to a fixed DMI is absent. This also suggests that thickness effects may play a role in the stabilization of the magnetic objects.

2.2. Thickness Dependence of Stripe Domains and Skyrmion Crystals

We observed that the size of both the stripe domains and bubble textures (w) are strongly correlated with the thickness (t) of the $CrBr_3$ films. Figure 2a illustrates the tendency of decreasing the size of stripes (Figure 2b–d), and SkX structures (Figure 2e–f) with the reduction of t. This behavior is obtained via both MFM measurements (ZFC, and FC at 50 mT) and micromagnetic simulations for the range of samples studied, which also followed a simple Kittel's law (e.g., $w \propto \sqrt{t}$, dashed line in Figure 2a). However, as the thickness reaches $t < 25$ nm, the trend rapidly reversed as the strong confinement changes the stability of the domain structure and associated spin textures. This behavior is in agreement with earlier theories and experimental reports[45,46] that pointed out the competition between magnetostatic and domain wall energies as one of the main ingredients.[47,48] Other additional effects at the few-layer limit, such as pinning or localized strains,[43] might become important on the stabilisation of the magnetic structures and could contribute to the divergence of Kittel's law. Such pinning centers were directly observed in bilayer $CrBr_3$ with NV-center magnetometry[43] with characteristic size of the pinned domains around several hundreds of nanometers.

The reproduction of the t-dependent sizes of the magnetization textures in micromagnetic simulations required t-dependent exchange constants as indicated in Table S2 (Supporting Information). The unique evolution of the magnetization textures with film thickness resulted in the identification of three different regimes characterised by specific characteristics of the magnetic structure and the formation of the skyrmions: ultrathin (Néel-like, $t = 3 - 25$ nm), intermediate (hybrid, $t = 28 - 105$ nm) and bulk-like (Bloch-like, $t > 110$ nm). Note that below 3 nm the system is in monodomain regime and skyrmions are not formed. Figure 2h–j shows the real space magnetization from micromagnetic simulations at different thicknesses (20, 100, and 200 nm) of the SkX generated at the surface with specific spin arrangements. It is worth mentioning that at $t < 20$ nm the exchange energy dominates all other energy terms. This interesting feature can be used to accurately determine the strength of the exchange constant for $CrBr_3$, which is a common practice in the micromagnetic thin film community.[44,46] For example, the frequency of spin waves undergoes a rapid increase towards infinity when approaching the exchange dominated region, as the thickness is decreased.[49] We can currently only speculate why this approach worked, but a larger effective exchange energy may indicate important

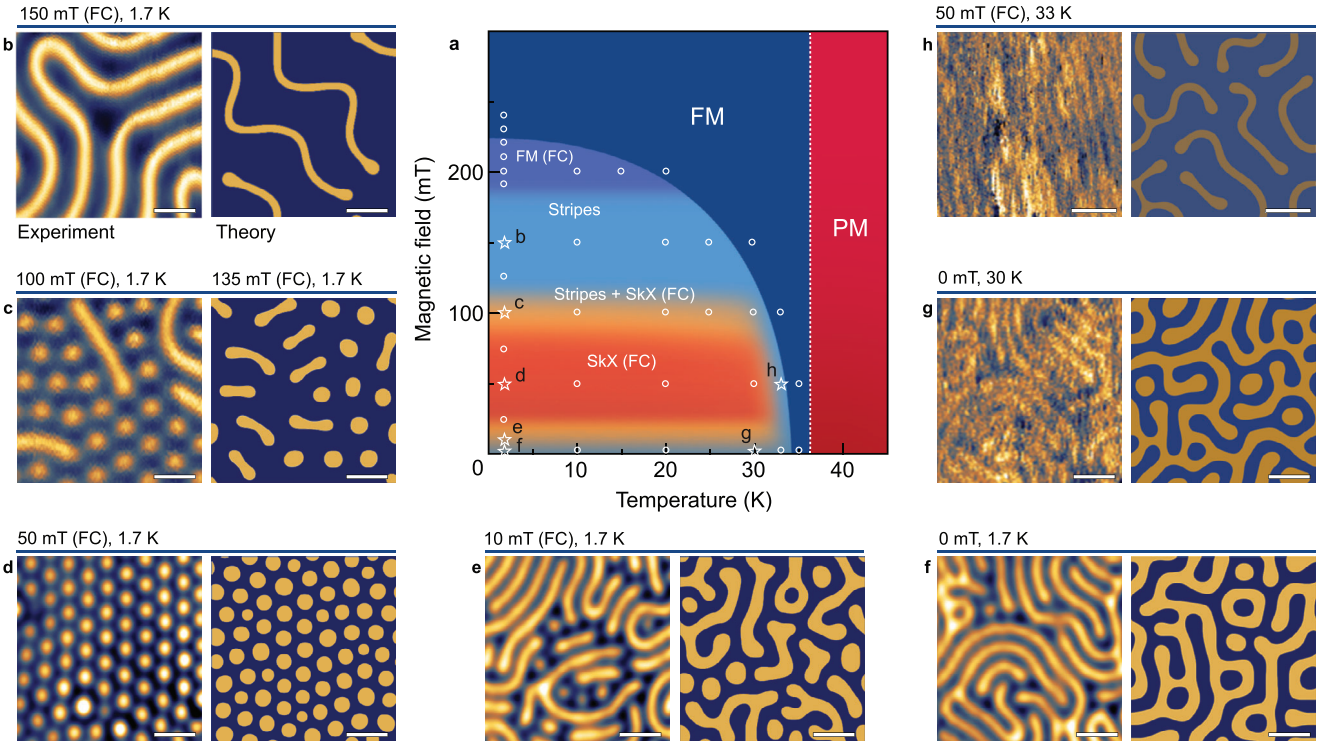

Figure 3. Coexistence of skyrmions, stripe domains and magnetic textures on a $T-B$ phase diagram. a) Phase diagram for the magnetic field (mT) versus temperature (K) was constructed based on magnetic force microscopy and micromagnetic simulations to demonstrate several phases involving skyrmion lattice (SkX), stripe ferromagnetic domains (FM), and their coexistence, e.g., Stripes + SkX. FC was used to stabilize ferromagnetic phases that contain skyrmion components. Paramagnetic (PM) state is shown for reference. b–h) Comparison between MFM measurements (left) and micromagnetic simulation (right) at specific conditions of temperature, field, and cooling protocols (FC, ZFC) marked with stars on the phase diagram: b) stripe domains after FC at 150 mT at 1.7 K; c) coexistence of stripes and skyrmions in case of FC done at 100 and 135 mT at 1.7 K; d) SkX after FC at 50 mT at 1.7 K; e) coexistence of stripes and skyrmions in case of smaller FC done at 10 mT and 1.7 K; f) stripe domains in case of ZFC and 1.7 K; g) stripe domains with reduced magnetization at 30 K; h) reemergence of stripe configuration in case of FC at 50 mT at higher temperatures of 33 K. Scale bar is 0.5 μm.

energy contributions from surface or interlayer pinning, which could become larger with stacking of additional layers.

2.3. $T-B$ Phase Diagram

The overall picture of the spin textures stabilized in $CrBr_3$ can be thoroughly described via a $T-B$ phase diagram including both ZFC and FC cases (**Figure 3a**). The extreme cases in the form of stripe domains, skyrmion lattice, and the hybrid scenarios involving their coexistence were soundly captured by both MFM and micromagnetic calculations (Figure 3b–h). In the ZFC case, only stripe domains were observed in the temperature range up to the Curie point (≈37 K). With the increase in temperature, the geometry of the pattern was preserved, while the contrast between the opposite domain regions decreased due to the thermal fluctuations and consequent reduction of the magnetization (Figure 3f,g). The stripe domains vanished close to the paramagnetic phase (PM) around 35 K, attributed here to the limited sensitivity from the tip of the MFM cantilever. In the presence of a magnetic field, the threshold temperature of stripe-domain disappearance decreases in agreement with well-known $M(T) = M(0)(1-(T/T_c)^{3/2})$ dependence for ferromagnetic materials.[48] The finite field also leads to modifications in the geometry of the magnetic structures. The stripe domains increase in their size in a manner that the domains co-oriented with the external field overcome anti-oriented stripe domains, eventually leaving several isolated bubbles at the fields close to the saturation (See Figure S4, Supporting Information).

The formation of non-trivial topological spin textures in well ordered SkX, occurred due to FC with fields within 25–75 mT (Figure 3d). SkX's are energetically stable in a large range of temperatures (1.7–30 K) preserving the point lattices (e.g., skyrmions) and their arrangements. At higher temperatures (e.g., 33 K), stripe domains were found to be preferable without the nucleation of skyrmions (Figure 3h), which is closely reproduced by the micromagnetic simulations. Strikingly, the FC protocol undertaken at magnetic fields outside of the SkX range, i.e., below 25 mT or above 75 mT, leads to hybrid magnetization patterns involving the coexistence of skyrmions and stripe domains in the surface. MFM and simulated magnetization images demonstrate examples of such configurations at 10 mT (Figure 3e) and 100 mT (Figure 3c) with different ratio of stripe domains to skyrmions. At higher magnetic fields (>100 mT) using FC, the magnetic order reenters into the stripe-dominant phase, which differs to similar situation at ZFC (e.g., Figure 3f,g) in terms of the field-induced modification of the domain sizes (Figure 3b) and the reduced saturation field. The

system was found to become completely magnetized (e.g., FM) at a magnetic field of 200 mT via FC. The specific details of the phase diagram inherently depend on the thickness of the $CrBr_3$ films (e.g., where each phase might be stabilized). Nevertheless, in a simple view, the saturation field correlates well with the thickness of the sample, thereby increasing the value of magnetic fields in FC required for the formation of SkX in thicker samples. It is noteworthy that each phase can be transformed into each other by tuning the field and temperature at an FC or ZFC situation. This indicates flexibility on the manipulation of a determined magnetic phase toward applications.

2.4. Using Photoluminescence to Probe Spin-Textures in $CrBr_3$

$CrBr_3$ as an insulator with planar ionic bonds, interlayer van der Waals coupling, and a host to a prolific number of spin textures, offers a unique platform to investigate the interplay between skyrmions and standard optoelectronic excitations. The strong correlations in the electronic system give rise to a large single-particle bandgap and large exciton binding energy.[50] This led to the observation of excitons localized down to a single $CrBr_3$ molecule limit in the form of mixed Frenkel and charge-transfer excitations. Consequently, the excitonic spin was found to be coupled with magnetization, enabling exciton spin pumping mechanisms.[50,51]

Here, we devised a protocol to observe the impact of skyrmions on the ferromagnetic hysteresis loops through magneto-photoluminescence spectroscopy resolved by circular polarization. The PL intensity curves, indicative of the magnetization averaged over the laser spot, were obtained using the following procedure. Initially, a field cooling process was performed at a specific magnetic field. Subsequently, the magnetic field was swept unidirectionally until saturation was reached, while simultaneously exciting the system with circularly polarized light and continuously monitoring the emitted light. Once the saturation was achieved, the full hysteresis loop was recorded. The sample was then heated above Curie's temperature, and another FC process was conducted in the same magnetic field. Following this, the magnetic field was swept in the opposite direction, until saturation was reached and the full hysteresis loop was recorded again for comparison. The experiment was done for several values of the FC field providing insights into how the initial state of the system influenced the behavior of the sample magnetization in the magnetic field.

Figure 4a–c displays the normalized PL intensity for three different cases of initial conditions highlighted by the orange dot at 0 T, 50 mT, and 120 mT, respectively. ZFC case with the usual strip domain configuration (Figure 4a) showed a symmetrical behavior of the black curve along both directions, with a saturation field of ≈200 mT. For the full hysteresis loop (blue and red curves in Figure 4a) saturation field is slightly larger, ≈225 mT. This slight increase in saturation field is expected, as an additional magnetic field is necessary to compensate for any remnant magnetization in the system. For the case with 50 mT FC corresponding to the SkX scenario (Figure 4b), the hysteresis loop exhibited notable changes. Initially, in the vicinity of the starting point, the magnetization tends to maintain its state, displaying minimal changes with the applied field. As the field increases, the shape of the curve becomes convex, attempting to follow the red and blue curves of the full hysteresis loop. Importantly, the curve is non-symmetric, with a significantly higher saturation field at one end. This asymmetry in the saturation field is a distinct feature of the SkX presence, in agreement with MFM measurements demonstrating that the orientation of the magnetization within skyrmionic bubbles is opposite to the direction of the FC field (see. Figure 4e for a schematic representation of the magnetization orientation and Figure 4f-n for MFM images of SkX at different external magnetic fields). For FC at 125 mT (Figure 4c), when the ground state is characterized by stripes, the black curve also exhibits asymmetries and looks distorted near the initial field. However, the saturation field is not as high as in the case of SkX. MFM scans of ZFC stripe domains and SkX behavior in the external magnetic field at 1.7 K can be found in Figures S4 and S5 (Supporting Information). It correlates with the observations from the PL intensity hysteresis curves.

A detailed summary of these magneto-optical measurements can be constructed via a phase diagram involving the saturation field and the applied FC field (Figure 4d). Such diagram was built from the MFM images (color-coded map) and the saturation field extracted from the magneto-PL spectroscopy (white open dots). The plot illustrates the dependence of the saturation field on the FC field and the corresponding initial state for one direction of the applied field. It is evident that the field required to fully magnetize the sample is highest in the case of the presence of the skyrmion lattice (>240 mT), which originally existed in the range of 25–75 mT for the investigated sample's thickness without the laser excitations (Figure 3a). The scenario involving stripe-skyrmion coexistence, as well as the case with stripe domains obtained during the FC experiment at higher fields, no longer exhibited the effect of an enhanced saturation field. The observed increase in the saturation field for skyrmions could be explained by their higher stability compared to other magnetic domains and constitutes unambiguous evidence of skyrmion–exciton coupling. As the magnetic field was increased, the concentration of skyrmions decreased (as observed in MFM images in Figure 4f–n), but the spin configuration of the remaining skyrmions remains preserved. However, when an opposite magnetic field was applied, there came a point where a "burst" occurred, and the skyrmions started to transform into bubbles. This transition led to a more volatile magnetic structure, as bubble domains are not characterized by the enhanced stability of skyrmions. Consequently, at higher magnetic fields, the system reached saturation at the usual, lower value. In this context, the probing of complex nanoscale magnetic objects via diffraction-limited optical techniques under continuous-wave laser excitation constitutes an appealing alternative towards detection and manipulation of magnetic topological states.

3. Conclusion

Our results pointed out $CrBr_3$ as a unique platform for hosting a skyrmion crystal stabilized via the interplay between dipolar field and exchange energy in an insulating environment. The weak interlayer vdW coupling enabled us to characterize the emerging magnetization textures in a broad range of film thicknesses, temperatures, and magnetic fields. These details provide a thorough picture of the mechanisms responsible for

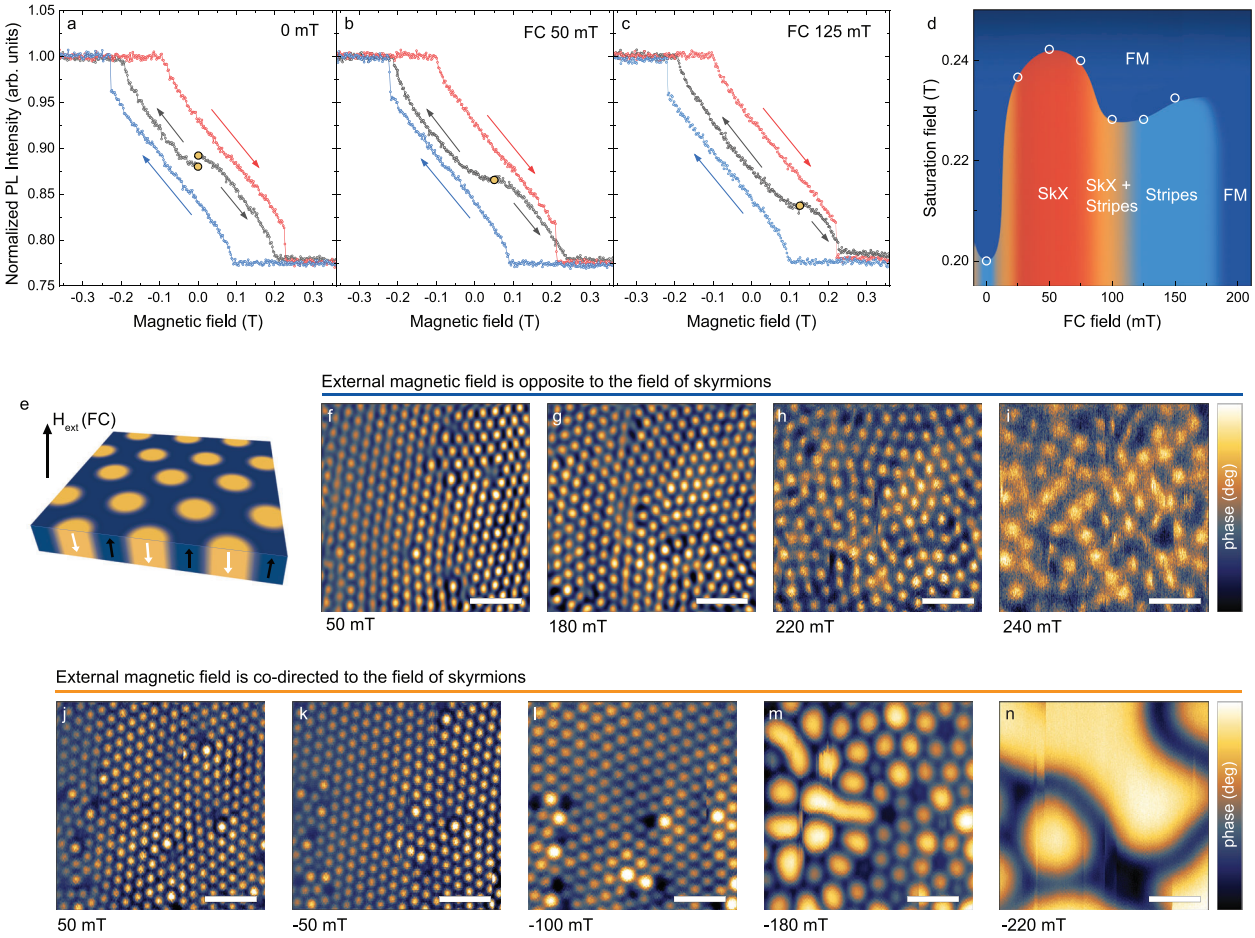

Figure 4. Photoluminescence intensity hysteresis loops revealing exciton–skyrmion coupling. Polarization–resolved normalized photoluminescence intensities captured from 170 nm thick $CrBr_3$ crystal during sweeping of the magnetic field. a–c) PL intensity as a function of a magnetic field for various cooling protocols: FC (a), 50 mT FC (b), and 125 mT FC (a). The magnetic field was swept several times in different directions as indicated by the color-coded arrows. The orange spot indicates the value of the magnetic field during FC and marks the starting point of the sweep for each experiment. d) Saturation field values for cases of different FC fields superimposed the phase diagram previously derived from magnetic force microscopy measurements. e) Schematic representation of magnetization arrangement in skyrmions relative to the direction of the FC field. f–n) MFM images of SkX, stabilized by 50 mT FC procedure, as a function of the external magnetic field directed opposite (f–i) or along (j–n) the magnetization of the skyrmions. The magnetization of skyrmions was always oriented in the opposite direction to the FC field. The scale bar corresponds to 1 µm.

stabilizing vastly different magnetic states determined by the physical conditions and the history of the sample. Some spin features such as dipole-stabilized Bloch-type skyrmion lattices with mixed chiralities display negligible Dzyaloshinskii–Moriya interactions. This presents as an exciting opportunity to engineer the formation and controllability of topological spin-textures on-demand accordingly to the target application. The 2D insulating character of $CrBr_3$ crystals will facilitate the integration of such hosts of skyrmionic lattices with memory and computing technology.[27] Further control knobs could be developed based on topological charge with significantly improved energy management and optical access enabled by large electronic band gap. It is important to remark that the formation of non-trivial magnetic textures on 2D vdW magnets has been almost exclusively reported so far on metallic materials (e.g., $Fe_{3-x}GeTe_2$, $Fe_{5-x}GeTe_2$), and a small-band gap semiconductor ($Cr_2Ge_2Te_6$), see Table S3 (Supporting Information) for a detailed review. The discovery of a broad horizon of topological magnetic objects and their manipulation via different external driving forces in $CrBr_3$ magnets opens a pathway for the development of low-power consumption device platforms. The next challenge however is to substantially increase the critical temperature of the magnetic ordering but keeping the outstanding spin features observed in our work. As the transition temperature of $CrBr_3$ is lower relatively to other 2D magnets,[32] one of the foreseen research directions would be the enhancement of their magnetic stability to room temperature, where real applications can be achieved. In principle, such process can be achieved via molecular intercalation.[52]

4. Experimental Section and Computational Methods

Sample Fabrication: The study was carried out comparatively using commercial $CrBr_3$ crystals purchased from HQ graphene and $CrBr_3$ crystals grown via a procedure described below. Both types of crystal exhibited the same types of magnetization texture and magneto-optical response in

identical physical conditions. Thin $CrBr_3$ was mechanically exfoliated on polydimethylsiloxane substrates in an inert gas glove box with a water and oxygen concentration of less than 0.5 ppm. $CrBr_3$ flakes were transferred on a pre-patterned gold electrode or on SiO_2/Si substrate at room temperature. The thicknesses of $CrBr_3$ flakes were first identified by optical contrast and then more precisely measured with an atomic force microscope (AFM). Thin layers were additionally encapsulated with few nm of hBN or graphite to prevent degradation. The samples were exposed to air for less than 10–15 min before being transferred to helium environment in the cryostat probe. Furthermore, the exposure of the samples to light was limited, as CrX_3 compounds demonstrated higher degradation rates under illumination. Detailed information on the structure of the samples and basic characterization including optical and atomic force microscopy imaging, height profiling, Raman scattering and photoluminescence spectroscopy are presented in Figures S2 and S3 (Supporting Information).

Crystal Growth: The stoichiometric ratio of Cr powder and Br_2 liquid was loaded into a silica tube, the end of which was immersed in liquid nitrogen to prevent Br_2 evaporation. The tube was then pumped to a pressure $<10^{-1}$ Pa and sealed. It was gradually heated for 3 days to 1000 °C and kept under such conditions for three days. Ultimately, bulk $CrBr_3$ single crystals were obtained in the tube.

Magnetic Force Microscopy: AFM and MFM measurements were performed using an attocube attoDRY 2100 closed-cycle cryogenic microscope with a base temperature of 1.66 K, equipped with a 9 T superconducting magnet. Silicon probes with magnetic CoCr-coating, with spring constant k of 2.5–5 N m^{-1}, and resonance frequency of 87–91 kHz (Nanoscope MFMR, MFMR-LM with lower magnetic moment and also SSS-MFMR for higher resolution for very thin samples) were used. The probes were magnetized at room temperature using a neodymium magnet. In the measurements, the magnetic contrast was observed in both tapping and non-contact lift modes in the phase signal. In non-contact regime the cantilever was held at constant height (lift) from 20 to 300 nm depending on the sample thickness and interaction with the domains. It was chosen to maximize sensitivity and reduce dragging of the domains due to interaction with MFM tip. Overall, lift was 20–30 nm for samples with thickness below 100 nm, for thicker samples lift was 50–80 nm. At magnetic fields close to saturation lift was increased up to 300 nm to reduce dragging effects. During the measurements the magnetic field was applied in out-of-plane direction.

Photoluminescence Measurements: Photoluminescence experiments were carried out in the same attocube attoDRY 2100 closed-cycle cryogenic system. Samples were mounted on piezoelectric stages allowing *x*–*y*–*z* positioning. The measurements were performed in a backscattering geometry, using a continuous wave excitation at 730 nm, with a laser power of ≈50 µW. The laser light was focused using an objective lens with a numerical aperture of 0.82 yielding a spot of ≈1 µm in diameter. The light emitted from the sample was collimated by the same objective and scattered by a 0.75-m spectrometer equipped with a 150 grooves mm^{-1} grating and a charge-coupled device camera. The magnetic field was applied to the sample in the out-of-plane direction through superconducting coils. In magneto-PL experiments, the sample was excited with circularly polarized laser light realized with a $\lambda/4$ wave plate placed in the excitation path.

Micromagnetic Simulations: To support the experimental results, micromagnetic simulations of $CrBr_3$ magnetic ground states were carried out using MuMax3.[53] The value for saturation magnetization was set to M_s = 270 kA m^{-1}, in accordance with measured values at low temperature.[54] The uniaxial magnetic anisotropy constant was assumed to be K_u = 86 kJ m^{-3} along the out-of-plane direction, which has been reported for bulk material.[54] A global exchange stiffness was estimated from the exponential rise of domain size to be A_{ex} = 1e-12 J m^{-1}, which is within the range of reported values 10^{-12}–10^{-14} J m^{-1} for $CrBr_3$.[43] The continuum interfacial DMI constant $D = 0.15 \times 10^{-3}$ J m^{-2} was derived from its ASD counterpart as follows $D_0 = aa_z \frac{D}{\sqrt{3}}$, where a and a_z are the lattice parameters in the atomic and interlayer plane, respectively, and D_0 = 0.22 meV.[55]

Brown's thermal equation was incorporated into the simulation by running the Landau–Lifshitz equation in the time-domain for 10 ns at different values of temperature. The experimentally measured thermal variation of $M_s(T)$ was incorporated into the simulation using data in Ref. [54] (see Supporting Information). The corresponding values for $K_u(T)$ were determined from the equation $[K_u/K_u(T)] = [M_s/M_s(T)]^3$ that predicts a rapidly decaying uniaxial magnetocrystalline anisotropy with increasing temperature. The thermal variation of DMI and A_{ex} were estimated from their mean field approximations, which predict an approximately squared dependence $[M_s/M_s(T)]^2$.[56,57] Subject to this set of equations, the simulations indicated that stripe domains were more stable than skyrmions at higher temperatures, followed by a stable ferromagnetic phase. This behavior was also observed when adopting more rapidly decaying models of interfacial DMI.[58] The agreement between simulation and experiment can be enhanced by incorporating structural defects and pinning effects into the simulations.

Lorentz Transmission Electron Microscopy: LTEM samples were created by dry-exfoliating $CrBr_3$ flakes from a bulk crystal onto a silicon nitride TEM membrane and were then capped with 2 nm of sputtered Pt to prevent charging in the TEM and degradation. Cryo-LTEM imaging was performed using a JEOL JEM-2100F TEM instrument using a Gatan double-tilt liquid helium holder. Imaging was performed in Lorentz mode, which has a residual magnetic field of 155 Oe. The magnetic field along the beam direction was increased by exciting the objective lens. The total electron phase shift through the material was reconstructed using the transport of intensity method and the open-source PyLorentz software.[59] After LTEM imaging, the sample was measured to be ≈100 nm thick using atomic force microscopy.

Supporting Information

Supporting Information is available from the Wiley Online Library or from the author.

Acknowledgements

This project was supported by the Ministry of Education (Singapore) through the Research Centre of Excellence program (grant EDUN C-33-18-279-V12, I-FIM). This research is supported by the Ministry of Education, Singapore, under its Academic Research Fund Tier 2 (MOE-T2EP50122-0012). Z.L. acknowledges the support from National Research Foundation, Singapore, under its Competitive Research Programme (CRP) (NRF-CRP22-2019-0007), the Singapore Ministry of Education Tier 3 Programme "Geometrical Quantum Materials" AcRF Tier 3 (MOE2018-T3-1-002). This material is based upon work supported by the Air Force Office of Scientific Research and the Office of Naval Research Global under award number FA8655-21-1-7026. E.J.G.S. acknowledges computational resources through CIRRUS Tier-2 HPC Service (ec131 Cirrus Project) at EPCC (http://www.cirrus.ac.uk) funded by the University of Edinburgh and EPSRC (EP/P020267/1); ARCHER UK National Supercomputing Service (http://www.archer.ac.uk) via Project d429. E.J.G.S. acknowledges the EPSRC Open Fellowship (EP/T021578/1), and the Edinburgh-Rice Strategic Collaboration Awards for funding support. Work from A.R.C.M., Y.L. A.K.P. and C.M.P. was funded by the US Department of Energy, Office of Science, Office of Basic Energy Sciences, Materials Science and Engineering Division. Use of the Center for Nanoscale Materials, an Office of Science user facility, was supported by the U.S. Department of Energy, Office of Science, Office of Basic Energy Sciences, under Contract No. DE-AC02-06CH11357. For the purpose of open access, the authors have applied a creative commons attribution (CC BY) licence to any author accepted manuscript version arising.

Conflict of Interest

The authors declare no conflict of interest.

Author Contributions

S.G., M.K., E.J.G.S, and K.S.N. conceived the project. S.G. performed low-temperature MFM experiments and analyzed the data. M.G. conducted

optical microscopy characterization and analyzed the data. Z.C. and M.S. fabricated the samples. Y.L., A.M., A.K.P.-L., and C.M.P. performed LTEM measurements. C.M. and E.J.G.S. performed the micromagnetic simulations and theoretical support. D.R. and L.Z grew bulk $CrBr_3$ crystals. S.G., M.G., M.K., and E.J.G.S. wrote the manuscript with inputs from all co-authors. All co-authors contributed to this work, read the manuscript, discussed the results, and agreed on the included contents.

Data Availability Statement

The data that support the findings of this study are available from the corresponding author upon reasonable request.

Keywords

ferromagnets, magnetic force microscopy, photoluminescence, skyrmions, topological spin textures

Received: November 10, 2023
Revised: January 9, 2024
Published online: March 4, 2024

[1] A. Fert, N. Reyren, V. Cros, *Nat. Rev. Mater.* **2017**, *2*, 17031.
[2] Y. Tokura, N. Kanazawa, *Chem. Rev.* **2021**, *121*, 2857.
[3] K. M. Song, J.-S. Jeong, B. Pan, X. Zhang, J. Xia, S. Cha, T.-E. Park, K. Kim, S. Finizio, J. Raabe, J. Chang, Y. Zhou, W. Zhao, W. Kang, H. Ju, S. Woo, *Nat. Electron.* **2020**, *3*, 148.
[4] S. S. P. Parkin, M. Hayashi, L. Thomas, *Science* **2008**, *320*, 190.
[5] S. Mühlbauer, B. Binz, F. Jonietz, C. Pfleiderer, A. Rosch, A. Neubauer, R. Georgii, P. Böni, *Science* **2009**, *323*, 915.
[6] X. Z. Yu, Y. Onose, N. Kanazawa, J. H. Park, J. H. Han, Y. Matsui, N. Nagaosa, Y. Tokura, *Nature* **2010**, *465*, 901.
[7] K. Karube, J. S. White, N. Reynolds, J. L. Gavilano, H. Oike, A. Kikkawa, F. Kagawa, Y. Tokunaga, H. M. Rønnow, Y. Tokura, Y. Taguchi, *Nat. Mater.* **2016**, *15*, 1237.
[8] S. Heinze, K. von Bergmann, M. Menzel, J. Brede, A. Kubetzka, R. Wiesendanger, G. Bihlmayer, S. Blügel, *Nat. Phys.* **2011**, *7*, 713.
[9] N. Romming, C. Hanneken, M. Menzel, J. E. Bickel, B. Wolter, K. von Bergmann, A. Kubetzka, R. Wiesendanger, *Science* **2013**, *341*, 636.
[10] I. Kézsmárki, S. Bordács, P. Milde, E. Neuber, L. Eng, J. White, H. Rønnow, C. Dewhurst, M. Mochizuki, K. Yanai, H. Nakamura, D. Ehlers, V. Tsurkan, A. Loidl, *Nat. Mater.* **2015**, *14*, 1116.
[11] S. Woo, K. Litzius, B. Krüger, M.-Y. Im, L. Caretta, K. Richter, M. Mann, A. Krone, R. M. Reeve, M. Weigand, P. Agrawal, I. Lemesh, M.-A. Mawass, P. Fischer, M. Kläui, G. S. D. Beach, *Nat. Mater.* **2016**, *15*, 501.
[12] T. Kurumaji, T. Nakajima, V. Ukleev, A. Feoktystov, T.-h. Arima, K. Kakurai, Y. Tokura, *Phys. Rev. Lett.* **2017**, *119*, 237201.
[13] M.-G. Han, J. A. Garlow, Y. Liu, H. Zhang, J. Li, D. DiMarzio, M. W. Knight, C. Petrovic, D. Jariwala, Y. Zhu, *Nano Lett.* **2019**, *19*, 7859.
[14] B. Ding, Z. Li, G. Xu, H. Li, Z. Hou, E. Liu, X. Xi, F. Xu, Y. Yao, W. Wang, *Nano Lett.* **2020**, *20*, 868.
[15] R. Chen, Y. Gao, X. Zhang, R. Zhang, S. Yin, X. Chen, X. Zhou, Y. Zhou, J. Xia, Y. Zhou, S. Wang, F. Pan, Y. Zhang, C. Song, *Nano Lett.* **2020**, *20*, 3299.
[16] J. Zang, M. Mostovoy, J. H. Han, N. Nagaosa, *Phys. Rev. Lett.* **2011**, *107*, 136804.
[17] O. Boulle, J. Vogel, H. Yang, S. Pizzini, D. de Souza Chaves, A. Locatelli, T. O. Menteş, A. Sala, L. D. Buda-Prejbeanu, O. Klein, M. Belmeguenai, Y. Roussigné, A. Stashkevich, S. M. Chérif, L. Aballe, M. Foerster, M. Chshiev, S. Auffret, I. M. Miron, G. Gaudin, *Nat. Nanotechnol.* **2016**, *11*, 449.
[18] D. Maccariello, W. Legrand, N. Reyren, K. Garcia, K. Bouzehouane, S. Collin, V. Cros, A. Fert, *Nat. Nanotechnol.* **2018**, *13*, 233.
[19] W. Münzer, A. Neubauer, T. Adams, S. Mühlbauer, C. Franz, F. Jonietz, R. Georgii, P. Böni, B. Pedersen, M. Schmidt, A. Rosch, C. Pfleiderer, *Phys. Rev. B* **2010**, *81*, 041203.
[20] C. Pfleiderer, T. Adams, A. Bauer, W. Biberacher, B. Binz, F. Birkelbach, P. Böni, C. Franz, R. Georgii, M. Janoschek, F. Jonietz, T. Keller, R. Ritz, S. Mühlbauer, W. Münzer, A. Neubauer, B. Pedersen, A. Rosch, *J. Phys.: Condens. Matter* **2010**, *22*, 164207.
[21] I. Raičević, D. Popović, C. Panagopoulos, L. Benfatto, M. B. Silva Neto, E. S. Choi, T. Sasagawa, *Phys. Rev. Lett.* **2011**, *106*, 227206.
[22] Y. Onose, Y. Okamura, S. Seki, S. Ishiwata, Y. Tokura, *Phys. Rev. Lett.* **2012**, *109*, 037603.
[23] K. S. Burch, D. Mandrus, J. G. Park, *Nature* **2018**, *563*, 47.
[24] M. Gibertini, M. Koperski, A. F. Morpurgo, K. S. Novoselov, *Nat. Nanotechnol.* **2019**, *14*, 408.
[25] C. Gong, X. Zhang, *Science* **2019**, *363*, 6428.
[26] K. F. Mak, J. Shan, D. C. Ralph, *Nat. Rev. Phys.* **2019**, *1*, 646.
[27] Q. H. Wang, A. Bedoya-Pinto, M. Blei, A. H. Dismukes, A. Hamo, S. Jenkins, M. Koperski, Y. Liu, Q.-C. Sun, E. J. Telford, H. H. Kim, M. Augustin, U. Vool, J.-X. Yin, L. H. Li, A. Falin, C. R. Dean, F. Casanova, R. F. L. Evans, M. Chshiev, A. Mishchenko, C. Petrovic, R. He, L. Zhao, A. W. Tsen, B. D. Gerardot, M. Brotons-Gisbert, Z. Guguchia, X. Roy, S. Tongay, et al., *ACS Nano* **2022**, *16*, 6960.
[28] Y. Wu, S. Zhang, J. Zhang, W. Wang, Y. L. Zhu, J. Hu, G. Yin, K. Wong, C. Fang, C. Wan, X. Han, Q. Shao, T. Taniguchi, K. Watanabe, J. Zang, Z. Mao, X. Zhang, K. L. Wang, *Nat. Commun.* **2020**, *11*, 3860.
[29] T.-E. Park, L. Peng, J. Liang, A. Hallal, F. S. Yasin, X. Zhang, K. M. Song, S. J. Kim, K. Kim, M. Weigand, G. Schütz, S. Finizio, J. Raabe, K. Garcia, J. Xia, Y. Zhou, M. Ezawa, X. Liu, J. Chang, H. C. Koo, Y. D. Kim, M. Chshiev, A. Fert, H. Yang, X. Yu, S. Woo, *Phys. Rev. B* **2021**, *103*, 104410.
[30] M. Augustin, S. Jenkins, R. F. L. Evans, K. S. Novoselov, E. J. G. Santos, *Nat. Commun.* **2021**, *12*, 185.
[31] J. Macy, D. Ratkovski, P. P. Balakrishnan, M. Strungaru, Y.-C. Chiu, A. Flessa Savvidou, A. Moon, W. Zheng, A. Weiland, G. T. McCandless, J. Y. Chan, G. S. Kumar, M. Shatruk, A. J. Grutter, J. A. Borchers, W. D. Ratcliff, E. S. Choi, E. J. G. Santos, L. Balicas, *Appl. Phys. Rev.* **2021**, *8*, 041401.
[32] B. W. Casas, Y. Li, A. Moon, Y. Xin, C. McKeever, J. Macy, A. K. Petford-Long, C. M. Phatak, E. J. G. Santos, E. S. Choi, L. Balicas, *Adv. Mater.* **2023**, *35*, 2212087.
[33] M. Khela, M. Dąbrowski, S. Khan, P. S. Keatley, I. Verzhbitskiy, G. Eda, R. J. Hicken, H. Kurebayashi, E. J. G. Santos, *Nat. Commun.* **2023**, *14*, 1378.
[34] D. A. Wahab, M. Augustin, S. M. Valero, W. Kuang, S. Jenkins, E. Coronado, I. V. Grigorieva, I. J. Vera-Marun, E. Navarro-Moratalla, R. F. Evans, K. S. Novoselov, E. J. G. Santos, *Adv. Mater.* **2021**, *33*, 2004138.
[35] Y. Gao, S. Yan, Q. Yin, H. Huang, Z. Li, Z. Zhu, J. Cai, B. Shen, H. Lei, Y. Zhang, S. Wang, *Phys. Rev. B* **2022**, *105*, 014426.
[36] R. Fujita, P. Bassirian, Z. Li, Y. Guo, M. A. Mawass, F. Kronast, G. van der Laan, T. Hesjedal, *ACS Nano* **2022**, *16*, 10545.
[37] J. Chen, L. Wang, M. Zhang, L. Zhou, R. Zhang, L. Jin, X. Wang, H. Qin, Y. Qiu, J. Mei, F. Ye, B. Xi, H. He, B. Li, G. Wang, *Nano Lett.* **2019**, *19*, 6144.
[38] D. Li, S. Haldar, S. Heinze, *Nano Lett.* **2022**, *22*, 7706.
[39] C.-K. Li, X.-P. Yao, G. Chen, *Phys. Rev. Res.* **2021**, *3*, L012026.
[40] W. Tang, H. Liu, Z. Li, A. Pan, Y.-J. Zeng, *Adv. Sci.* **2021**, *8*, 2100847.
[41] M. Strungaru, M. Augustin, E. J. G. Santos, *npj Comput. Mater.* **2022**, *8*, 169.

[42] B. Huang, G. Clark, E. Navarro-Moratalla, D. R. Klein, R. Cheng, K. L. Seyler, D. Zhong, E. Schmidgall, M. A. McGuire, D. H. Cobden, W. Yao, D. Xiao, P. Jarillo-Herrero, X. Xu, *Nature* **2017**, *546*, 270.
[43] Q.-c. C. Sun, T. Song, E. Anderson, A. Brunner, J. Förster, T. Shalomayeva, T. Taniguchi, K. Watanabe, J. Gräfe, R. Stöhr, X. Xu, J. Wrachtrup, F. Johannes, *Nat. Commun.* **2021**, *12*, 1.
[44] S. A. Montoya, S. Couture, J. J. Chess, J. C. T. Lee, N. Kent, D. Henze, S. K. Sinha, M.-Y. Im, S. D. Kevan, P. Fischer, B. J. McMorran, V. Lomakin, S. Roy, E. E. Fullerton, *Phys. Rev. B* **2017**, *95*, 024415.
[45] F. Virot, L. Favre, R. Hayn, M. Kuz'Min, *J. Phys. D: Appl. Phys.* **2012**, *45*, 405003.
[46] I. Lemesh, F. Büttner, G. S. D. Beach, *Phys. Rev. B* **2017**, *95*, 174423.
[47] J. A. Cape, G. W. Lehman, *J. Appl. Phys.* **2003**, *42*, 5732.
[48] A. Hubert, R. Schäfer, *Magnetic Domains: The Analysis of Magnetic Microstructures*, Springer, Berlin, Germany **1998**.
[49] V. Sluka, T. Schneider, R. A. Gallardo, A. Kákay, M. Weigand, T. Warnatz, R. Mattheis, A. Roldán-Molina, P. Landeros, V. Tiberkevich, A. Slavin, G. Schütz, A. Erbe, A. Deac, J. Lindner, J. Raabe, J. Fassbender, S. Wintz, *Nat. Nanotechnol.* **2019**, *14*, 328.
[50] M. Grzeszczyk, S. Acharya, D. Pashov, Z. Chen, K. Vaklinova, M. van Schilfgaarde, K. Watanabe, T. Taniguchi, K. S. Novoselov, M. I. Katsnelson, M. Koperski, *Adv. Mater.* **2023**, *35*, 2209513.
[51] E. Sutcliffe, X. Sun, I. Verzhbitskiy, T. Griepe, U. Atxitia, G. Eda, E. J. G. Santos, J. O. Johansson, *Phys. Rev. B* **2023**, *107*, 174432.
[52] H. Iturriaga, L. M. Martinez, T. T. Mai, A. J. Biacchi, M. Augustin, A. R. Hight Walker, M. F. Sanad, S. T. Sreenivasan, Y. Liu, E. J. G. Santos, C. Petrovic, S. R. Singamaneni, *npj 2D Mater. Appl.* **2023**, *7*, 56.
[53] A. Vansteenkiste, J. Leliaert, M. Dvornik, M. Helsen, F. Garcia-Sanchez, B. Van Waeyenberge, *AIP Adv.* **2014**, *4*, 107133.
[54] N. Richter, D. Weber, F. Martin, N. Singh, U. Schwingenschlögl, B. V. Lotsch, M. Kläui, *Phys. Rev. Mater.* **2018**, *2*, 1.
[55] D. Cortés-Ortuño, W. Wang, M. Beg, R. A. Pepper, M.-A. Bisotti, R. Carey, M. Vousden, T. Kluyver, O. Hovorka, H. Fangohr, *Sci. Rep.* **2017**, *7*, 4060.
[56] L. Rózsa, U. Atxitia, U. Nowak, *Phys. Rev. B* **2017**, *96*, 094436.
[57] U. Atxitia, D. Hinzke, O. Chubykalo-Fesenko, U. Nowak, H. Kachkachi, O. N. Mryasov, R. Evans, R. W. Chantrell, *Phys. Rev. B* **2010**, *82*, 134440.
[58] S. Schlotter, P. Agrawal, G. S. Beach, *Appl. Phys. Lett.* **2018**, *113*, 092402.
[59] A. R. McCray, T. Cote, Y. Li, A. K. Petford-Long, C. Phatak, *Phys. Rev. Appl.* **2021**, *15*, 044025.